fluids

MDPI

Article

Spatiotemporal Analysis of Transient Liquid Film Shape

Gašper Vidic [1], Saša Bajt [2,3] and Božidar Šarler [1,*]

[1] Department of Fluid Dynamics and Thermodynamics, Faculty of Mechanical Engineering, University of Ljubljana, Aškerčeva 6, 1000 Ljubljana, Slovenia; gasper.vidic@fs.uni-lj.si
[2] Center for Free-Electron Laser Science CFEL, Deutsches Elektronen-Synchrotron DESY, Notkestr. 85, 22607 Hamburg, Germany; sasa.bajt@desy.de
[3] The Hamburg Centre for Ultrafast Imaging, Luruper Chaussee 149, 22761 Hamburg, Germany
* Correspondence: bozidar.sarler@fs.uni-lj.si

Abstract

Precise control of thin liquid film deposition is crucial in applications where film stability and internal liquid flow significantly impact the dry film shape or the efficiency of sample or drug delivery. No prior work has automated the extraction and measurement uncertainty quantification of film geometric parameters from dual-view optical visualization with minimal user input. We present Python-based software that extracts time-resolved film thickness, width, and the positions of three contact lines from visual data using computer vision. The utility of such analysis is demonstrated by depositing 30% glycerol on a flexible tape through a circular nozzle orifice. The nozzle is positioned at a distance of $h = 0.3$ mm from the tape at an angle of attack $\alpha = 45^\circ$, with deposition controlled at a volume flow rate $\dot{V} = 30\ \mu\text{L min}^{-1}$ and tape velocity $v = 1.0$ mm s^{-1}. Expanded measurement uncertainties are 21 µm, 22 µm, and 53 µm for the upstream static, downstream static, and upstream dynamic contact line positions, respectively, with maximum relative uncertainties of 10.3% and 8.2% for film thickness and width. Static contact line oscillations remain within measurement uncertainty, whereas the upstream dynamic contact line exhibits resolvable oscillations. This dual-view framework provides high-resolution insights into liquid film dynamics, which is crucial for comprehensive control of liquid film deposition.

Keywords: liquid film shape; dual-view imaging; optical visualization; automated spatiotemporal analysis

1. Introduction

Thin liquid films are important to the production of many products, such as organic light-emitting diode screens [1,2], lithium-ion battery electrodes [3,4], photovoltaic cells [5], fuel cells [6–9], transdermal patches [10,11], and buccal films [12]. In these products, internal liquid flow and film stability during deposition significantly impact the dry film shape and its functional properties [13–17]. Liquid films are also essential in the TapeDrive [18–21]—a conveyor-based sample delivery system commonly used in serial crystallography experiments, a novel method in structural biology that utilizes synchrotron sources to determine high-resolution molecular structures. In these experiments, samples are transported within a thin liquid film into the X-ray beam. Precise and stable delivery is crucial for preserving sample integrity and preventing mechanical damage or excessive sample soaking. Across these applications, flow dynamics near the film edge influence the film shape and internal liquid flow [22–25]. These effects induce transient geometric fluctuations, which impact deposition stability and the concentration and spatial distribution of the sample or the drug.

Check for updates

Academic Editors: Jay Tang, Van-Tu Nguyen and Hemant J. Sagar

Received: 2 February 2026
Revised: 24 February 2026
Accepted: 28 February 2026
Published: 3 March 2026

https://doi.org/10.3390/fluids11030067

Therefore, an accurate characterization of geometric parameters during the deposition process is critical.

Geometric parameters can be analyzed by visualization, interferometry, or laser profiling. Film thickness, width and edge width measurements are typically performed using an interferometer [26–28] or a high-speed 2D/3D laser profiler [22,23,29–31] with a micrometer or nanometer accuracy. Visualization of the side view was first done qualitatively using dyes in slide coating by Schweizer [32], where he also discussed, but did not quantify, the optical distortion caused by the curved liquid–gas interface of the film. Much research has been conducted on the positions of contact lines [33–37] from recorded images. However, these studies relied on manual measurements, and none addressed measurement uncertainty.

In this paper, we present an experimental setup and software that enables the automatic, simultaneous dual-view spatiotemporal analysis of film geometric parameters, along with the quantification of the measurement uncertainty. The software also enables automatic extraction of geometric parameters from side-view images. Previously, the use of side-view data was limited not by edge detection capability but by the lack of quantified measurement uncertainty, which made such data unreliable for analysis. Although geometric parameter extraction in plan-view images [38] and side-view images [39] has been demonstrated, our approach uniquely provides simultaneous dual-view measurements together with their quantified uncertainties. This capability is essential for reliable interpretation of experiments and for validating computational fluid dynamics models. The automated dual-view analysis of film geometric parameters also provides instantaneous values of film geometric parameters, which are essential for predicting the possible occurrence of vortices inside the film [40]. Our novel experimental approach is specifically compatible with the continuous slot-die coating technique, which aims to form a stable and uniform film on a moving flexible tape.

2. Materials and Methods

This section is organized into two subsections. The first subsection describes the experimental setup and the rationale behind its components, followed by an explanation of the assembled optical setup. In the second subsection, we provide an overview of the software used for digital processing of visual data and an example of its logical functioning.

The parameters and key terminology used in this article are illustrated schematically in Figure 1a,b. We monitor the film thickness, width, and positions of three contact lines during the deposition process: the upstream static contact line (USCL), the downstream static contact line (DSCL), and the upstream dynamic contact line (UDCL). Figure 1a illustrates the USCL and DSCL as positive and negative distances, respectively, relative to the corresponding nozzle shoulders. The angle of attack of the nozzle shown in Figure 1a,b is represented by a positive value.

2.1. Experimental Setup

The experimental setup consists of two optical breadboards (I, III), an optical enclosure (VII), 3D-printed support structures, two translation stages (II, XI), a hydraulic system, an optical system, and a control system, schematically shown in Figure 2a. An enlarged section view, A-A, focusing on the nozzle (XIV) and its surroundings, is shown in Figure 2b. The entire setup is assembled on a large optical breadboard (I). Except for a few optical components, the whole experimental setup is optically enclosed (VII; Thorlabs, XE25C10D/M, Bergkirchen, Germany) to reduce the influx of contaminants into the system. The liquid is pushed through hydraulic tubes (Festo, PUN-4X0,75-BL, Ljubljana, Slovenia) on a moving tape and into the nozzle feeding capillary using a syringe pump (XIII; Harvard Apparatus, Pump 33 DDS (Dual Drive System) Syringe Pump, Holliston, MA, USA). The tape (DuPont, Kapton polyimide tape, Leeds, UK) is oriented horizontally, and its velocity is controlled by a stepper motor (X; AzureFilm, Creality Stepper Motor 42-34, Sežana, Slovenia) driven by a driver (AzureFilm, Motor Driver TB6600) at 1/32 micro-stepping to minimize vibrations caused by the motor's jerky movements. The velocity, acceleration, and direction of the stepper motor's spinning are controlled using the Accelstepper Arduino library [41]. The tape is under tension and limited in movement in both vertical and lateral directions by a 3D-printed support structure, produced using a Prusa i3 MK3S+ printer (Prusa Research, Prague, Czech Republic); however, its tension is not controlled. The support structure and the stepper motor did not come into contact, which reduced vibration propagation from the stepper motor to the tape.

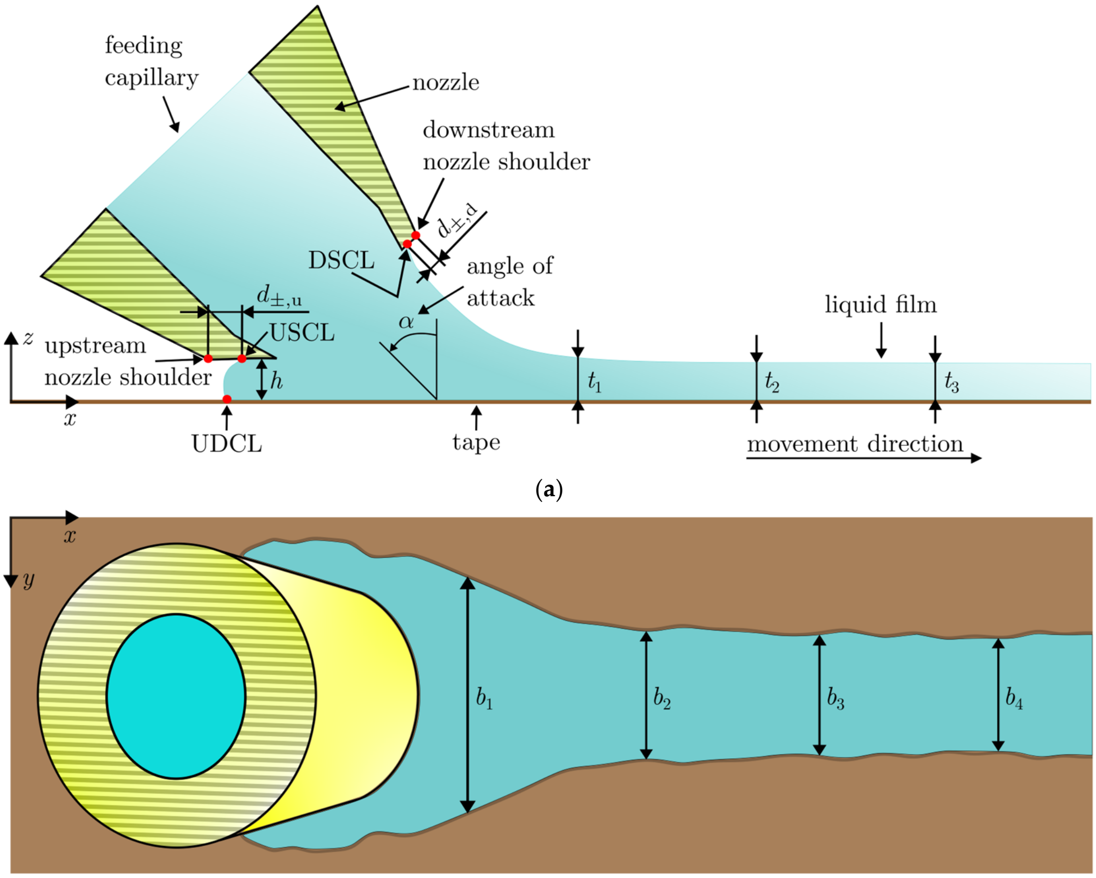

(**a**)

(**b**)

Figure 1. A schematic representation of geometric parameters and key terminology in (**a**) side view and (**b**) plan view.

The monochromatic camera (V; Pixelink, PL-D755MU-T, Rochester, NY, USA) and optical microscope (IV; Qioptiq, Saint Asaph, UK), which enable up to 12.5 times magnification, are positioned on a smaller optical breadboard (III). The latter component is mounted on a lab jack (II, Thorlabs, L200/M, Bergkirchen, Germany) to enhance handling and facilitate better vertical positioning for video acquisition. The camera is connected to a computer (VI), on which we save the video recordings of the measurements. The nozzle (XIV) is mounted on a three-axis translation stage (XI; Thorlabs, LX30/M, Bergkirchen, Germany), which ensures accurate positioning of the nozzle in the x, y, and z axes. A goniometer (XII; Thorlabs, PR01/M, Bergkirchen, Germany) is used to set its angle of attack. The stepper motor transfers its momentum to the wheel, causing it to move the tape. After the liquid moves past the region of interest, it is disposed of into a liquid container box

(XV) located outside the optical enclosure. Figure 2b shows section view A-A, illustrating the nozzle position relative to the support structure. It also illustrates how the tape tension is regulated, laterally constrained, and moved by the wheels with angular frequency w.

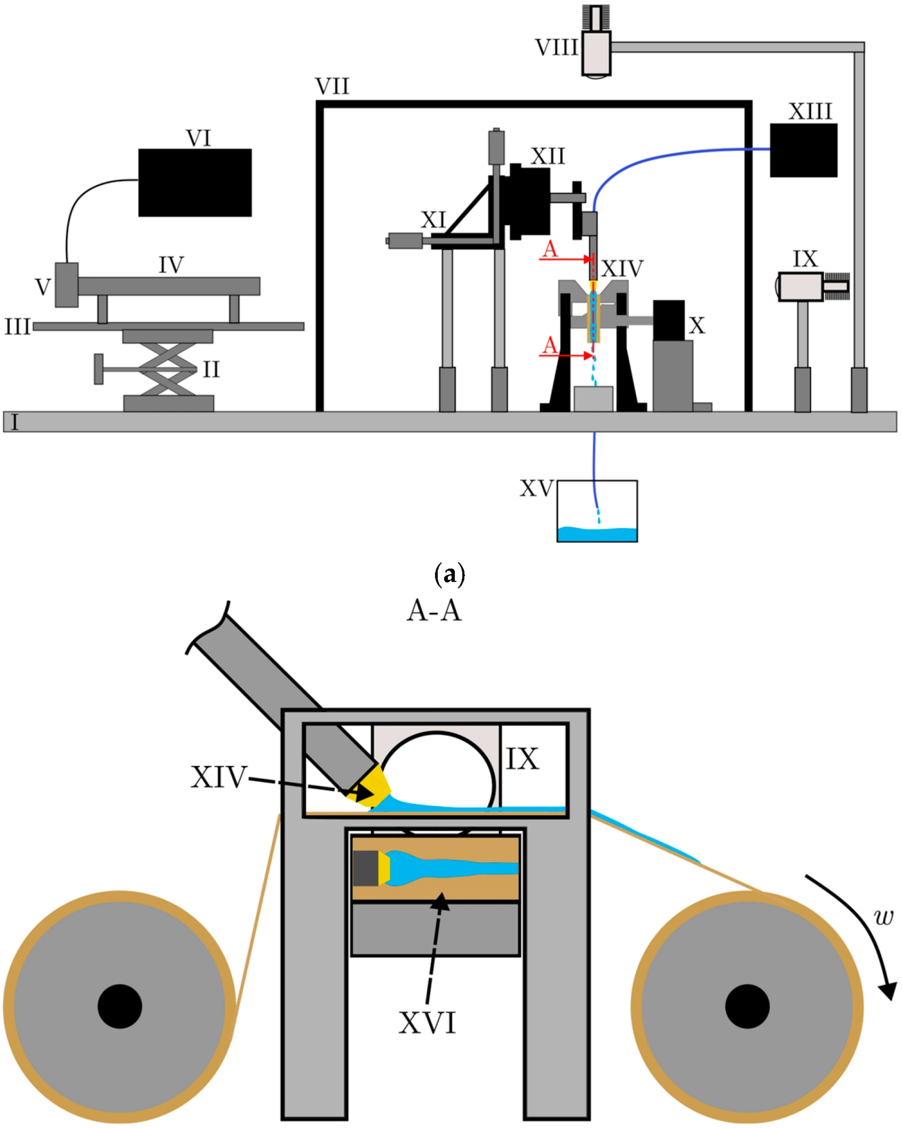

(**a**)

(**b**)

Figure 2. Schematic representation of (**a**) whole experimental setup: (I) optical breadboard 1, (II) lab jack, (III) optical breadboard 2, (IV) optical microscope, (V) monochromatic camera, (VI) computer, (VII) optical enclosure, (VIII) light source 1, (IX) light source 2, (X) stepper motor, (XI) three-axis translation stage, (XII) goniometer, (XIII) pump, (XIV) nozzle, (XV) liquid container box. Schematic representation of (**b**) section view A-A showing the nozzle, its surrounding structures, and (XVI) reflective mirror.

Simultaneous imaging of side and plan views is achieved using a reflective mirror (XVI) tilted at an angle $\varphi = 45^\circ$. The optical system utilizes two collimated LED (Light-Emitting Diodes) light sources (VIII, IX; Thorlabs, MCWHL8-C1, Bergkirchen, Germany). A plan view image is illuminated using light source VIII, and the side view using light source IX. Figure 3 illustrates the tape and deposited film from a plan view, showing the positioning of the optical setup within the experimental arrangement. The directions of light emitted from the light sources are indicated by two red lines.

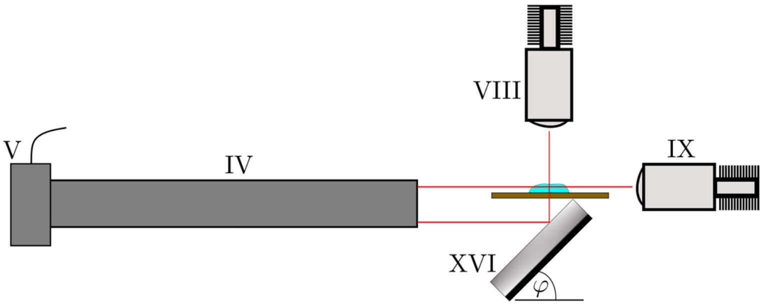

Figure 3. Schematic representation of optical setup: (V) monochromatic camera, (IV) optical microscope, (VIII) light source 1, (IX) light source 2, (XVI) reflective mirror.

In the presented study, we use a nozzle with a circular orifice, 3D-printed with a Micro microSLA printer (Kudo3D, Dublin, CA, USA) with a resolution of 10 μm in the z-axis. Figure 4 shows an isometric view of the nozzle geometry with hidden lines visible. Visible edges are drawn as solid lines, and hidden edges as dashed lines. The feeding capillary diameter D_c, the orifice exit diameter D_o, and the upstream and downstream bottom surface lengths L_u and L_d are indicated. As shown in Figure 4, the feeding capillary is axisymmetric, while the outer nozzle geometry is not.

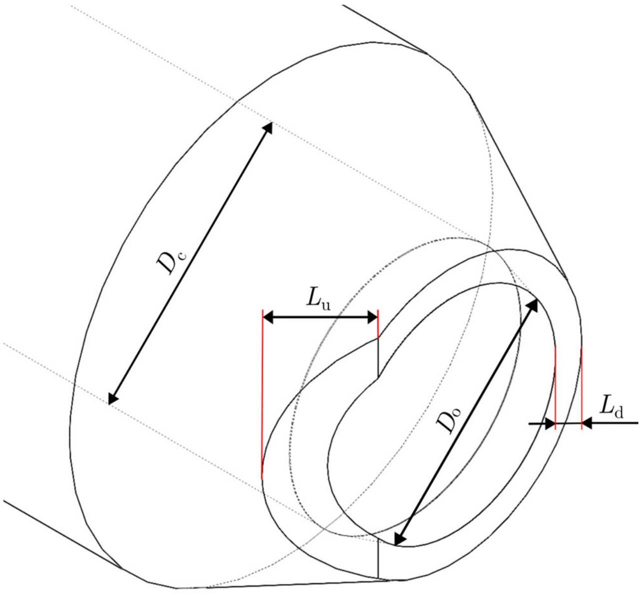

Figure 4. Isometric view of the nozzle geometry CAD model in SOLIDWORKS 2024 with hidden lines visible. Its dimensions are D_c = 2.40 mm, D_o = 2.12 mm, L_u = 1.39 mm, and L_d = 0.27 mm.

The highest step rate of a stepper motor achievable with the Arduino Uno R3 (16 MHz clock) microcontroller board (AzureFilm, Sežana, Slovenia) is approximately 4000 steps per second. In our setup, we use 1/32 microstepping to minimize vibrations, which translates to 6400 steps per complete wheel revolution. Theoretically, the minimum step rate with the Accelstepper library is 0.00027777 steps per second [41]. Given our wheel diameter of 70 mm, the corresponding reliable speed range at 1/32 microstepping is approximately 10 nm s^{-1} to 3.44 cm s^{-1}. The maximum and minimum speeds could also be altered by reducing the microstepping ratio or using a different wheel diameter. Volume flow rate-wise, we are limited by the syringe pump to minimum and maximum volume flow rates of 1.02 pL min^{-1} and 106 mL min^{-1}.

2.2. Digital Processing

Measurements are recorded using a single monochromatic camera, producing vast amounts of visual data that are then digitally processed. Each video consists of 79 frames (this value was chosen arbitrarily) with a resolution of 2448 × 2048 pixels, resulting in 396,361,728 processed pixels per video. The related software receives video as input and outputs spatiotemporally analyzed geometric parameters. Digital processing is divided into pre-processing, processing and post-processing, as shown in Figure 5.

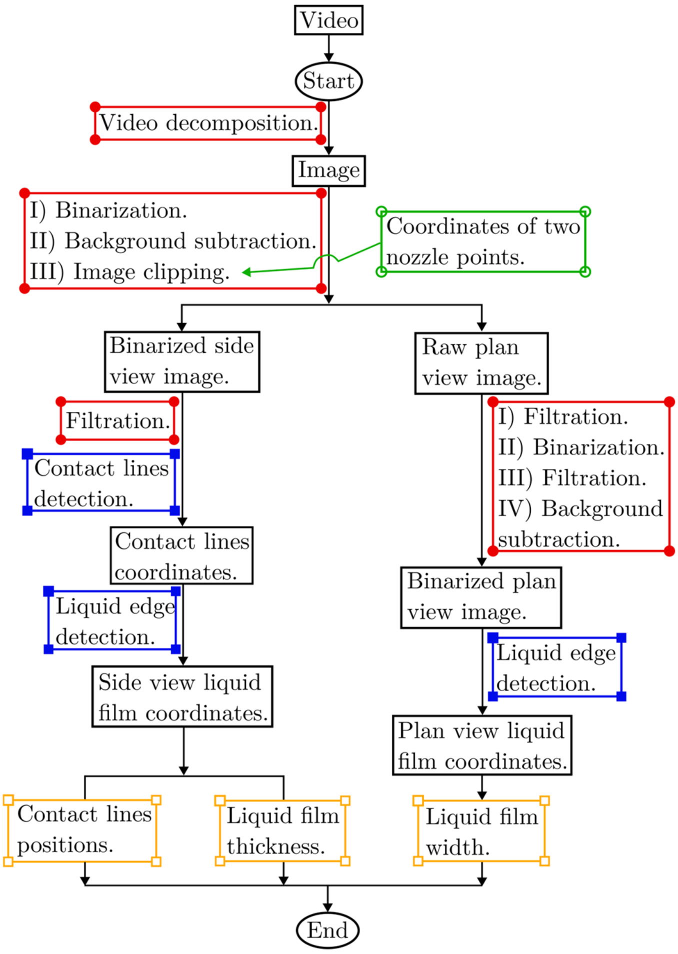

Figure 5. Schematic description of the whole digital processing of a single video.

Although this processing course is the same for both views, the algorithms differ considerably between the side and plan views. A recorded video is first decomposed into individual frames. Each frame is processed as an image and undergoes binarization, background subtraction, and image clipping to isolate the two views, which are then processed separately. This pre-processing, with slight additional filtering, is sufficient for the side view; however, the plan view requires additional steps due to diffuse light reflections over the tape. After that, film edges are detected in both views, and the contact lines are identified in the side view. Finally, post-processing is performed to extract the desired geometric parameters. Pre-processing algorithms are represented in Figure 5 by red rectangles with solid circles at their vertices, and processing algorithms by blue rectangles with solid squares at their vertices. A green rectangle with hollow circles at its vertices signifies the required manual user input. The software relies partially on the following computer vision libraries: OpenCV [42], SciPy [43] and NumPy [44]. It also relies on a small part of an internal, unpublished library developed by members of our laboratory to perform binarization, which is accomplished using the Scikit-Image library [45], as well as the decomposition of videos into images. The resulting geometric parameters are visualized using the Matplotlib library [46].

In the following, we demonstrate the performance of the software and analyze geometric parameters for 30% glycerol deposition on a flexible Kapton polyimide tape. The liquid is deposited at a volume flow rate of $\dot{V} = 30\ \mu\mathrm{L\ min}^{-1}$, tape velocity is $v = 1.0\ \mathrm{mm\ s}^{-1}$, and the distance between the nozzle and the tape is $h = 0.3$ mm, with the nozzle positioned at an angle of attack $\alpha = 45°$. The experiment is conducted under ambient pressure and temperature $T = 20\ °\mathrm{C}$, with density $\rho = 1072.7\ \mathrm{kg\ m}^{-3}$, dynamic viscosity $\mu = 2.50$ mPa s, and surface tension $\sigma = 0.0702\ \mathrm{N\ m}^{-1}$. Capillary number is calculated as

$$\mathrm{Ca} = \frac{\mu v}{\sigma}, \tag{1}$$

and its value for our experiment is 4×10^{-5}.

2.2.1. Pre-Processing

The software first decomposes the video into individual subsequent images. These images are then binarized with Otsu's thresholding [47], an image segmentation method that automatically determines the optimal threshold value. After binarization, background subtraction is performed for both experimental and background images, as shown in Figures 6a and 6b, respectively. The background image shows the experimental setup in its stationary state, with no tape movement or liquid deposition. The same background image is used for the whole video, provided that the optical system and nozzle placement remain unchanged.

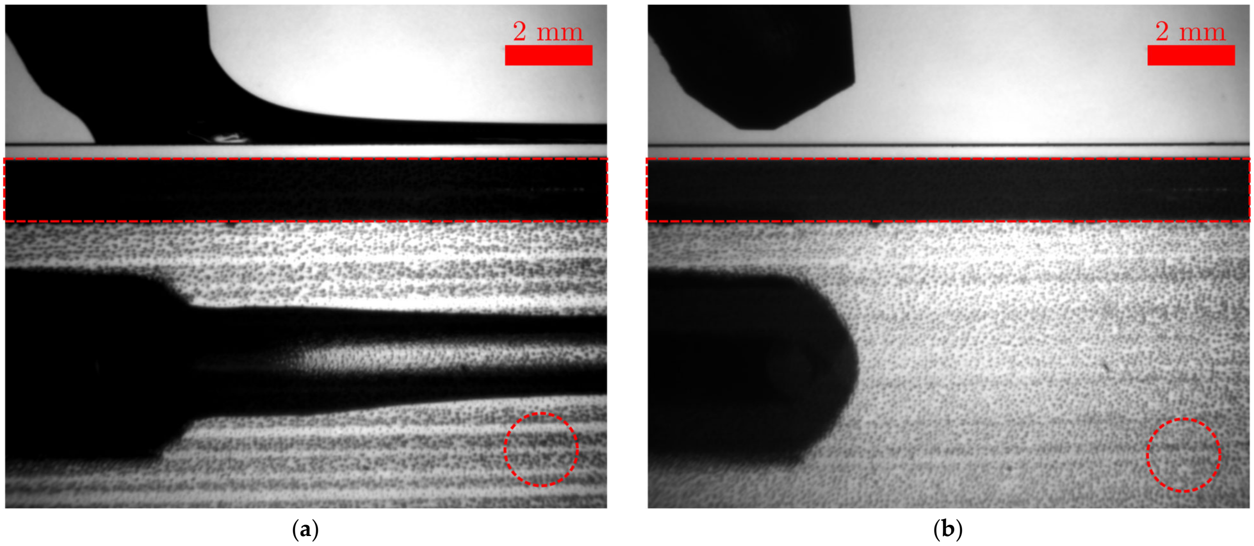

Figure 6. (**a**) An experimental image and (**b**) a background image. Red dashed rectangles highlight the non-reflective back side of the reflective mirror, and red dashed circles highlight surface unevenness.

Following background subtraction, images are clipped into two regions corresponding to side and plan views. The image clipping algorithm is a multi-step process, with the first step requiring manual user input of the position coordinates of two arbitrarily chosen points on the nozzle in side view. These points are selected as the upstream and downstream nozzle shoulders, represented by white plus signs in Figure 7. A white full line geometrically connects the two points, and a red dash-dotted line is drawn perpendicularly through its midpoint. The intersection between the red line and the tape's upper surface is then identified, which is marked by a yellow cross in Figure 7. Before completing image clipping, the region of interest is reduced by excluding the non-reflective back side of the reflective mirror, which is seen as a black rectangle highlighted by a red dashed rectangle in Figure 6a,b. The expected film width is estimated to narrow the region of interest further, and rows outside this range are omitted. A safety margin is included to ensure complete film capture in both views despite the detected camera tilt. After image clipping, the side and plan views are processed separately.

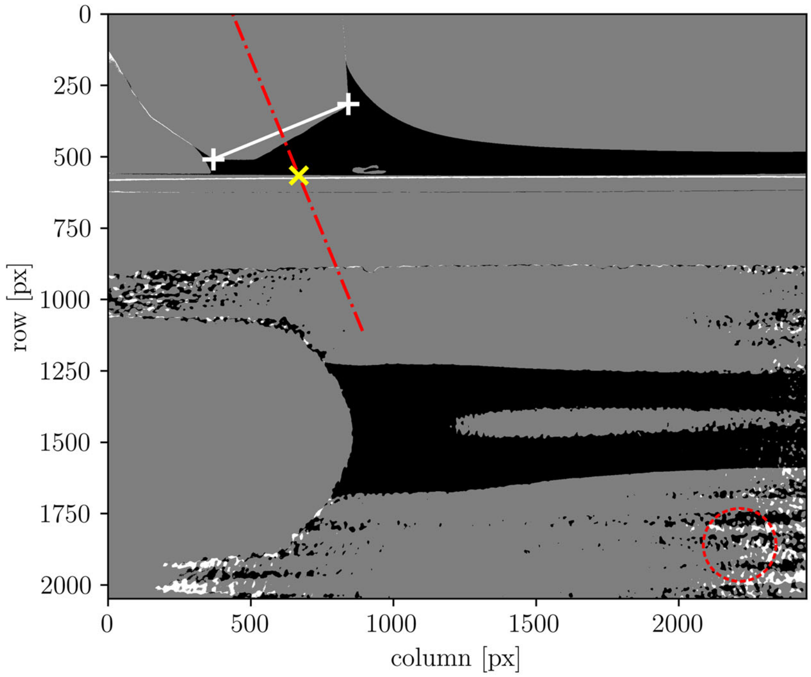

Figure 7. Image clipping. White plus signs, connected by a white full line, represent the upstream and downstream nozzle shoulders, and the yellow cross sign represents the intersection between the red dash-dotted line and the tape's upper surface. The red dashed circle highlights surface unevenness.

The side view requires only a slight filtration, as the minimal change in nozzle location during operation is negligible. The plan view, however, requires additional pre-processing due to light-scattering reflections produced by the uneven tape surface, as seen in Figures 6 and 7. Red dashed circles highlight examples of this unevenness in both figures. The striped and circular features represent variations in surface topography, visible in Figure 6a,b, and their effect on binarization is seen in Figure 7 as black and white dots—remnants of the surface unevenness. In both views shown in Figures 6a and 7, parts of the film appear as if no liquid is present because light passes through regions with minimal refraction. In plan view, this is evident in the central region of the film, where its surface is relatively flat. Pre-processing for the plan view is reinitiated from the raw image, consisting of a first filtration stage, Otsu's binarization, an additional second filtration, and finishing with background subtraction. The two filtering stages are performed using a morphological binary dilation operation with a square structuring element of 30 pixels in edge length.

2.2.2. Processing

We proceed with the processing algorithms. We acquire the film edges and the positions of three contact lines: UDCL, USCL, and DSCL. These contact lines are represented by red circles, green squares, and blue diamonds in Figure 8a. Film edges in side and plan views are shown in Figures 8b and 8c, respectively. The software first locates the film edge for the side view and then extracts the positions of the contact lines. For film edge detection, the algorithm first applies a small morphological operation to the image to remove noise resulting from minimal nozzle location changes, using a 5×5 pixel morphological matrix for UDCL extraction and a 3×3 pixel morphological matrix for USCL and DSCL. If required, these parameters can be easily changed. Next, the film edge is identified by detecting white pixels bordering black regions. Specifically, a pixel is classified as an edge if at least one of its eight neighboring pixels is black. The acquired film edge is shown in Figure 8b. To detect the upstream dynamic contact line, the algorithm first locates the tape position and then calculates the distance between each tape position and the film edge position. The upstream dynamic contact line is defined as the point where the distance between the tape and the film edge equals zero. Both static contact lines are detected in an image containing the nozzle, film edge, and tape. They are identified as points on the film edge with at least three adjacent black pixels. To avoid misidentifying the tape edge, a threshold is applied to exclude points that satisfy these conditions but correspond to the tape.

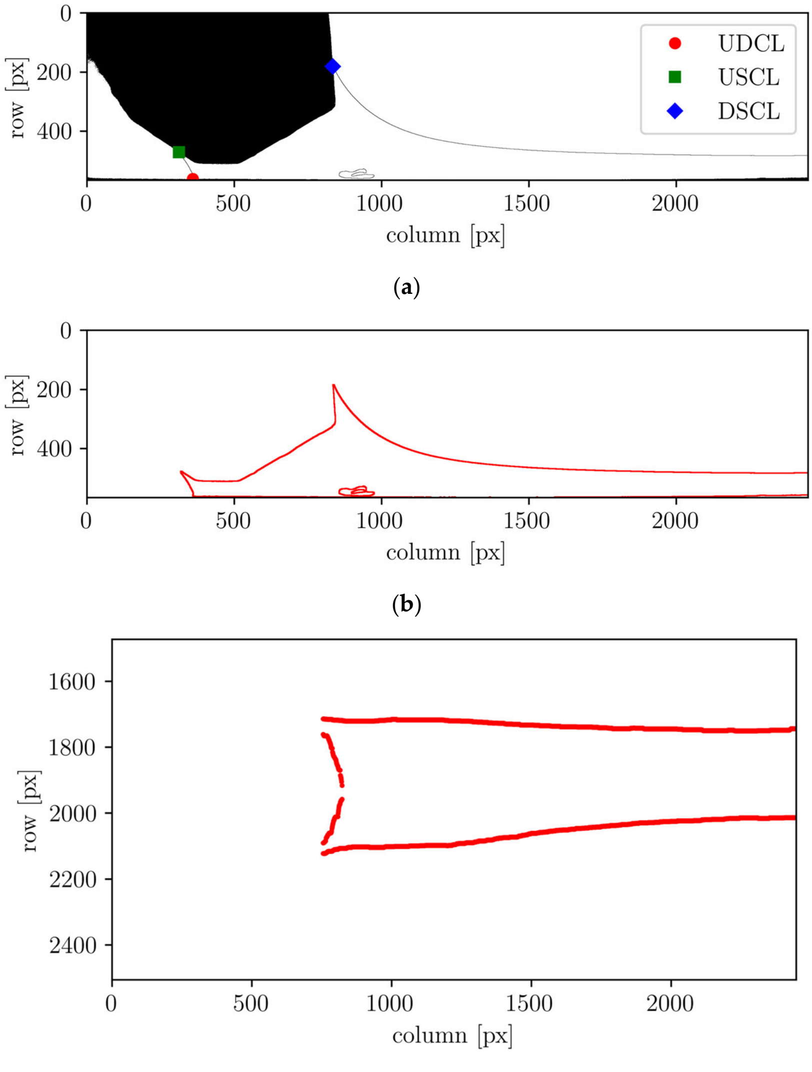

(**a**)

(**b**)

(**c**)

Figure 8. (**a**) Contact lines positions in side view, where the red circle, green square, and blue diamond represent UDCL, USCL, and DSCL, respectively. Film profile in (**b**) the side view, and (**c**) in the plan view.

For the plan view, only film edges are extracted. There, the film edge must first be separated from the nozzle edge, which is achieved by locating the points at which the film overlaps with the nozzle edge. The two points are identified to overlap when they are within a specified radius of 25 pixels. After acquiring overlapping points, the points corresponding to the film's edge are isolated. The resulting film edge in the plan view is shown in Figure 8c.

2.2.3. Post-Processing

After acquiring contact lines and film edges from both views, an extraction of geometric parameters is initialized. We focus on film thickness t, width b, UDCL x position, USCL to upstream nozzle shoulder distance $d_{\pm,\mathrm{u}}$, and DSCL to downstream nozzle shoulder distance $d_{\pm,\mathrm{d}}$.

Film thickness calculations account for camera tilt, which causes the tape to appear slanted, as illustrated in the magnified view of the tape in Figure 9a. To correct this, the tape's static position is recorded without liquid deposition, and this reference position is assumed to remain unchanged throughout the experiment.

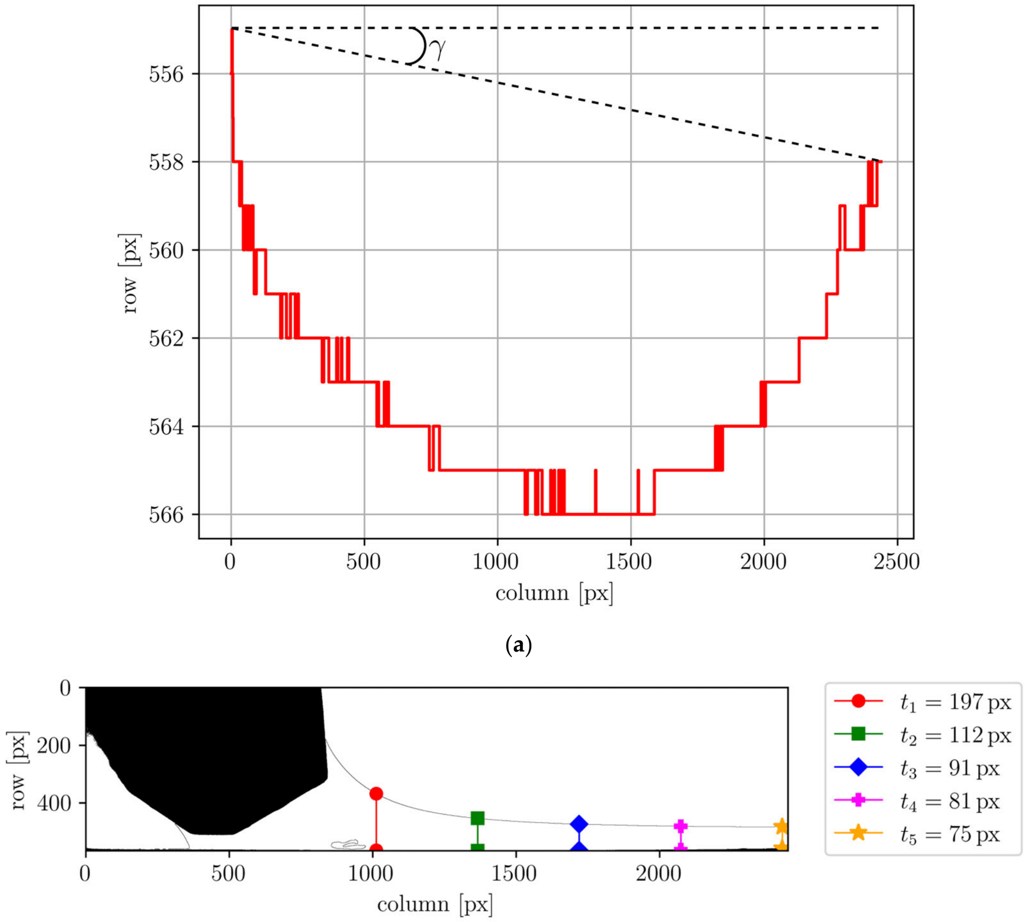

(**a**)

(**b**)

Figure 9. (**a**) Upper surface of moving tape. (**b**) Example of calculated liquid film thickness for one image. Film thickness measurement locations are annotated, and the corresponding values are indicated in the legend.

Film thickness is calculated in every column from DSCL downstream by subtracting the tape's row coordinate from the film edge's row coordinate in the same column and multiplying these results by the cosine of the tape's slope angle $\gamma = -0.07°$. A selection of measured film thicknesses is shown in Figure 9b, with annotated measurement locations and corresponding values indicated in the legend. A limitation of film's 2D projections, as seen with a camera, is the assumption that film thickness peaks at the midpoints, which may not capture full 3D variations.

Film widths are calculated as the difference between the row positions of the two liquid edges at each column, starting from the first film edge point at the nozzle and continuing downstream. We acquire instantaneous widths for every single positional increment, as shown in Figure 10, where the blue line represents the instantaneous film width and the dashed black line represents the first film edge point on the nozzle.

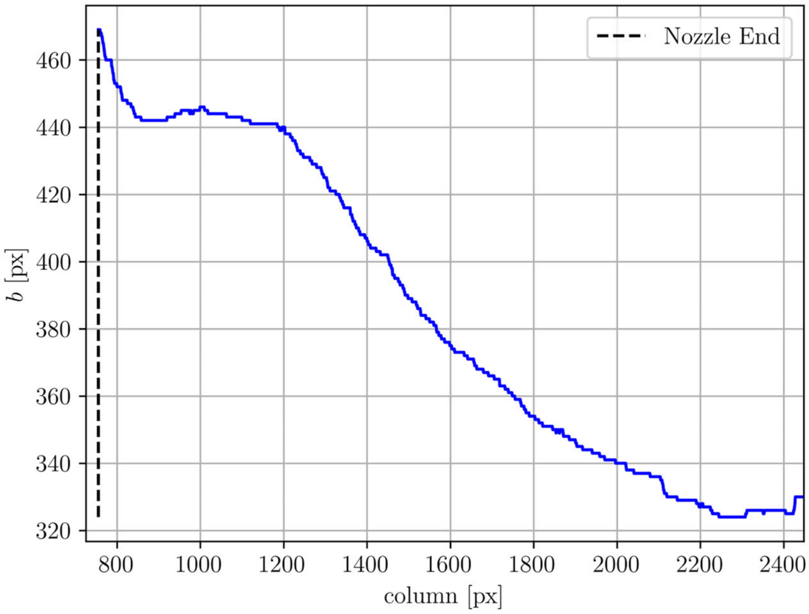

Figure 10. Instantaneous film widths at every positional increment, represented by a blue full line. The black dashed line is the first film edge point at the nozzle.

We also compute the minimum and maximum values of spatiotemporally dependent widths, along with their standard deviations. A relative distance between USCL and the upstream nozzle shoulder distance is evaluated with the equation:

$$d_{\pm,\mathrm{u}} = \sqrt{(x-x_0)^2 + (z-z_0)^2}\mathrm{sng}(x-x_0), \tag{2}$$

where x and z are nozzle shoulder coordinates, and coordinates x_0 and z_0 are the positions of USCL. The relative distance between DSCL and the downstream nozzle shoulder distance is evaluated with a similar equation:

$$d_{\pm,\mathrm{d}} = \sqrt{(x-x_0)^2 + (z-z_0)^2}\mathrm{sng}(z_0-z), \tag{3}$$

where coordinates x_0 and z_0 represent the positions of DSCL. Coordinates of the nozzle shoulders in Equations (2) and (3) are measured using the ImageJ program, version 1.54p [48].

We also calculated expanded measurement uncertainty for each geometric parameter. The coverage factor used in this calculation is determined using the effective degrees of freedom, obtained from the Welch–Satterthwaite formula [49–51]:

$$\nu_{\mathrm{eff}} = \frac{u_{\mathrm{c}}^4(Y)}{\sum_{i=1}^{N} \frac{u_{\mathrm{i}}(Y)}{\nu_{\mathrm{i}}}}, \tag{4}$$

where ν_{i} are degrees of freedom, Y is the output estimate of a measurand, and u_{c} is the combined standard uncertainty, calculated as:

$$u_\mathrm{c}^2(y) = \sum_{i=1}^{N} c_\mathrm{i}^2 u^2(x_\mathrm{i}), \tag{5}$$

with $u(x_\mathrm{i})$ denoting the standard uncertainty of the input estimate x_i. The coverage factor for a 95.45% confidence level is then obtained from the JCGM 100:2008 standard [52]. For this calculation, Type A contributions to measurement uncertainty are evaluated from frequency distributions, while Type B contributions are based on a priori distributions. We assume degrees of freedom $\nu_\mathrm{i} = 78$, corresponding to 79 frames per video, and consider only Type A contributions to the standard uncertainty in the denominator, which is calculated as the temporal standard deviations of the geometric parameters. Type B contributions are not included in the denominator, as they have infinite degrees of freedom ($\nu_\mathrm{i} = \infty$). For the combined standard uncertainties (u_c), we incorporate the contributions of the optical system to measurement uncertainty from image reprojections, binarization, filtration, and resolution as Type B contributions. Their variances are summed with the Type A contribution, and the square root of this sum yields the measurement uncertainty for each geometric parameter.

3. Results and Discussion

In this section, we present the results of measurements conducted under the same process (geometric, and rheological) conditions as described in the Methods and discuss their meaning. The visual data is digitally processed using software for automated image processing, which analyzes recordings of liquid deposition on a moving tape simultaneously from two views. We report the spatiotemporal evolution of film thickness, width, and contact lines positions, along with their variability and corresponding expanded measurement uncertainties. These results provide insight into the film's dynamic behavior and an assessment of the advantages and limitations of extracting film geometric parameters from video recordings using the presented automatic method combined with measurement uncertainty quantification.

3.1. Film Thickness

Quantitative film thickness analysis is conducted based on the processed side-view images, enabling the evaluation of spatial and temporal trends. We are not interested in a specific average value but in temporal oscillations and deviations. To capture this, we calculate temporally averaged film thicknesses at every positional increment along with corresponding minimum, maximum, and standard deviation values, as shown in Figure 11. Minimum and maximum values are indicated by green triangles and red dots, respectively. The light blue contour represents one standard deviation, and a black dashed line marks the position of DSCL. A zero value represents the temporally averaged film thickness at every positional increment.

As shown in Figure 11, the maximum deviation of measured film thickness from the temporal average is 36.0 µm, with a maximum standard deviation of 21.6 µm.

3.2. Film Width

Film width calculations are also based on images acquired from a plan view. We first calculate the temporal averages, minimums, maximums, and standard deviations of upper and lower film edge profiles. The maximum standard deviations for the upper and lower profiles are 30.6 µm and 43.8 µm, respectively. Averaged values and deviations of these two edge profiles are used to calculate the averaged values and deviations of the film width, assuming that the film edge profiles are independent.

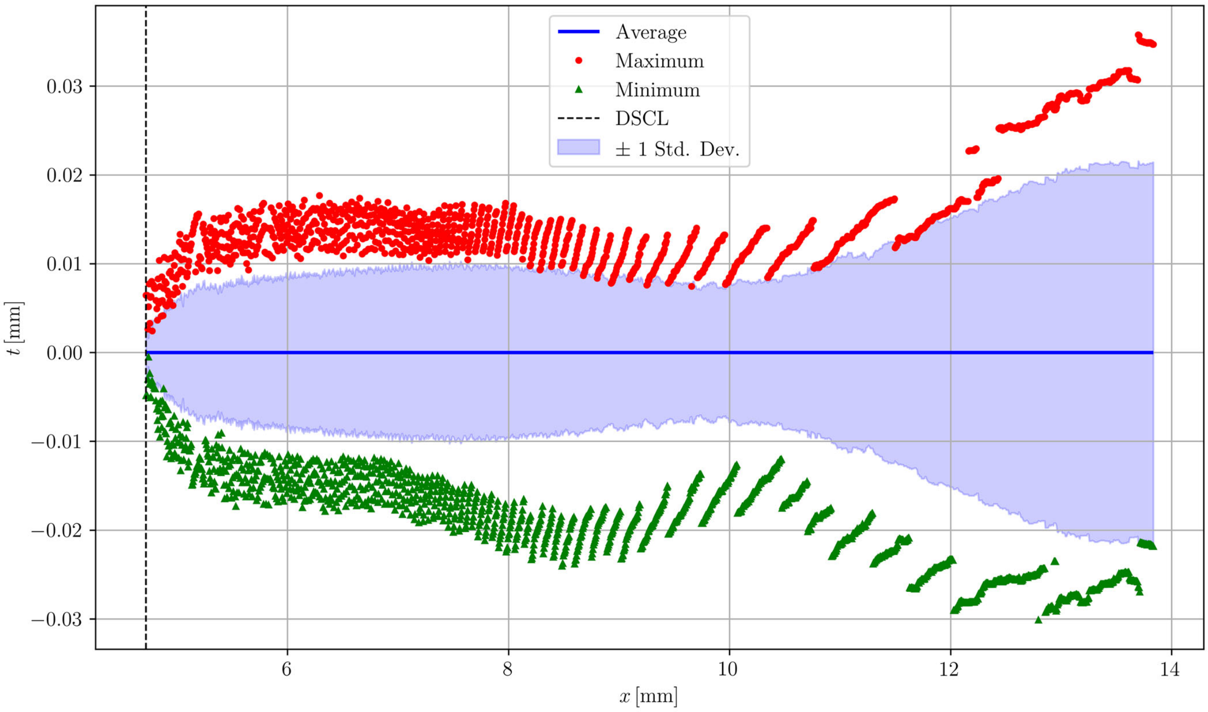

Figure 11. Temporally averaged film thickness and its deviations. A full blue line represents the temporally averaged value at every positional increment. Minimum and maximum values are indicated by green triangles and red dots, respectively. The light blue contour represents one standard deviation, and the black dashed line represents the DSCL.

The resulting temporally averaged width, minimum, maximum, and standard deviation values are shown in Figure 12. The maximum combined standard deviation from the two edges equals 53.0 µm.

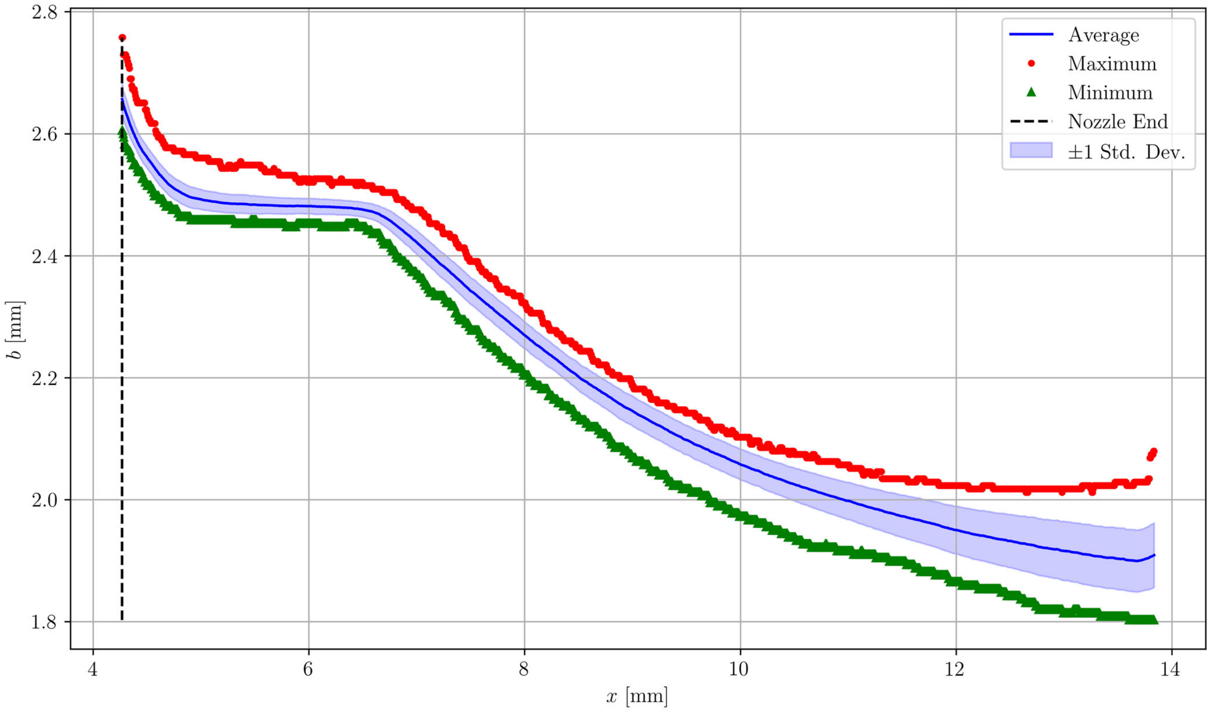

Figure 12. Temporally averaged film width and its deviations. Minimum and maximum values are represented by green triangles and red dots, respectively. The light blue contour represents one standard deviation, and the black dashed line marks the first film edge point at the nozzle.

3.3. Contact Lines Positions

Finally, we examine the movement between the static contact lines and the corresponding nozzle shoulder, as well as the movement of the upstream dynamic contact line. Their measured values are shown in Figure 13 as a function of the video frames N. Red triangles and blue dots in Figure 13 indicate distances between USCL and the upstream nozzle shoulder and between DSCL and the downstream nozzle shoulder, respectively.

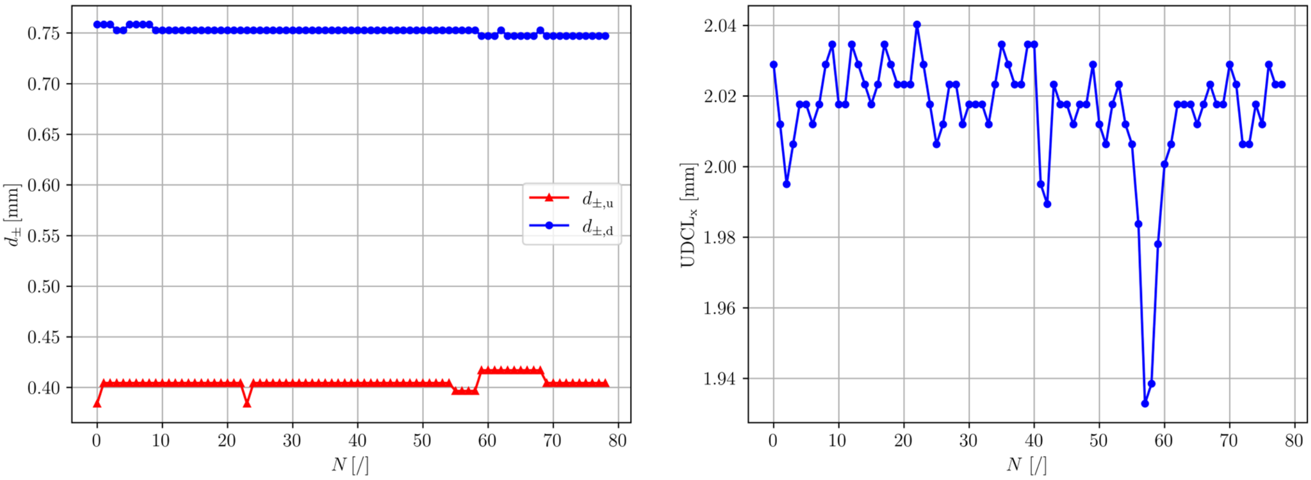

(**a**) (**b**)

Figure 13. Contact lines positions as a function of video frames N. (**a**) Distances between the USCL and the upstream nozzle shoulder and between the DSCL and the downstream nozzle shoulder are represented by red triangles and blue dots, respectively. (**b**) Oscillations of UDCL x component positions.

The calculated distances shown in Figure 13a indicate that the positions of USCL and DSCL oscillate around the mean value. Both distances are positively valued. The average distance between USCL and the upstream nozzle shoulder is 41 µm, with a standard deviation of 5.8 µm. In contrast, the average value between DSCL and the downstream nozzle shoulder is 75 µm, with a standard deviation of 3.1 µm. Although these parameters are expected to remain static, the observed standard deviations indicate otherwise.

The position of UDCL varies considerably more than the two static contact lines, as is evident in Figure 13b. Its average value is 2018 µm, with a standard deviation of 17.0 µm. Although oscillations exhibited very low standard deviation, Figure 13b shows that this movement is inherently dynamic.

3.4. Expanded Measurement Uncertainty

We calculate effective degrees of freedom for all geometric parameters using Equations (4) and (5). The lowest value of effective degrees of freedom was 172 for the film width. For effective degrees of freedom exceeding 100, a coverage factor of 2.000, corresponding to a 95.45% confidence interval, may be adopted in accordance with the JCGM 100:2008 standard [52]. Therefore, the dataset size of 79 frames is in our case sufficient to justify the assumption of a normal distribution in the statistical analysis of all geometric parameters. Expanded measurement uncertainties are then calculated for all geometric parameters. The uncertainties are 21 µm and 22 µm for USCL and DSCL to nozzle shoulder distances, respectively, and 53 µm for $\mathrm{UDCL_x}$. Oscillations in the distances between USCL and DSCL, as well as their corresponding nozzle shoulders, are observed in Section 3.3. However, these variations remain within the bounds of expanded measurement uncertainty and, therefore, cannot be reliably distinguished from Type B contributions. In contrast, the oscillations in the UDCL position exceed the expanded measurement uncertainty, indicating that its dynamic movement can be resolved through side-view analysis. The maximum expanded relative standard deviations are 10.3% for film thickness and 8.2% for width. Comparing the combined measurement uncertainties with the Type A components (see Appendix A) discussed in previous subsections, we calculate that Type B sources account for 44.1% and 71.3% of the uncertainties in USCL and DSCL distances to the nozzle shoulder, respectively, and 34.8% for $\mathrm{UDCL_x}$. For film thickness and width, Type B contributions amount to 18.7% and 73.4%, respectively. These results strongly suggest that Type B contributions must be considered in the analysis of geometric parameters. Additional information about the measurement uncertainty calculation procedure is laid out in Appendix A.

Measuring film thickness and width using interferometry or laser profiling is more accurate than the method presented here. However, these two methods cannot be used to extract contact lines positions.

Contact lines positions can be extracted using a visualization-based method, but this is done manually from recorded images. The achievable spatial resolution is fundamentally limited by the image pixel resolution. While measurement uncertainty could, in principle, be estimated using similar principles as in our method, manual extraction introduces an additional, operator-dependent variable. Reproducing results based on measurements taken by different people and across large datasets typical of parametric analyses and optimization studies is therefore very challenging. Using automatic extraction of contact lines from recorded images avoids these issues.

4. Conclusions

This study presents a framework for dual-view automated, temporally resolved analysis of liquid film geometry. Coupled with comprehensive measurement uncertainty quantification, it enables accurate, fast, and consistent high-resolution tracking of film thickness, width, and contact lines positions. Automated extraction of contact lines from side-view images improves measurement uncertainty assessment by overcoming the limitations of manual evaluation, which cannot fully account for optical distortions caused by the curved liquid–gas interface.

While the experiment was conducted under stable flow conditions, other liquid films may exhibit much higher variability due to differing liquid and substrate properties. Part of this software has already been utilized in several publications to analyze the geometric parameters of sample delivery systems, such as liquid jets, sheets, and films [53–56], underscoring the relevance of such analysis. Future developments will incorporate additional post-processing features, such as upstream and downstream meniscus curvatures. We demonstrate that automated dual-view analysis provides precise visualization-based characterization of transient liquid films, offering improved film quality control and optimization of dry film functional properties, as well as the efficiency of sample or drug delivery, in both scientific and industrial applications.

Author Contributions: G.V.: Conceptualization, Data Curation, Formal Analysis, Investigation, Methodology, Software, Visualization, Writing—Original Draft. S.B.: Conceptualization, Writing—Review and Editing, Funding Acquisition. B.Š.: Conceptualization, Writing—Review and Editing, Resources, Supervision, Project Administration, Funding Acquisition. All authors have read and agreed to the published version of the manuscript.

Funding: Funding for this research is provided by the Centre for Free-Electron Laser Science (CFEL) under the project: Innovative Methods for Imaging with the use of X-ray Free-Electron Laser (XFEL) and Synchrotron Sources: Simulation of Gas-focused Micro-jets; the Slovenian Grant and Innovation Agency (ARIS) [core funding P2-0162, project J2-4477]; the Young Researcher Program; and the Cluster of Excellence "CUI: Advanced Imaging of Matter" of the Deutsche Forschungsgemeinschaft (DFG) [EXC 2056, project ID: 390715994].

Institutional Review Board Statement: Not applicable.

Informed Consent Statement: Not applicable.

Data Availability Statement: The data that support the findings of this study are available from the corresponding author upon reasonable request.

Conflicts of Interest: The authors declare no conflicts of interest. The funders had no role in the design of the study; in the collection, analyses, or interpretation of data; in the writing of the manuscript; or in the decision to publish the results.

Abbreviations

The following abbreviations are used in this manuscript:

2D	Two-Dimensional
3D	Three-Dimensional
UDCL	Upstream dynamic contact line
DDS	Dual Drive System
DSCL	Downstream static contact line
LED	Light-Emitting Diode
USCL	Upstream static contact line

Appendix A

The combined standard measurement uncertainty is evaluated in accordance with the JCGM 100:2008 standard [52], incorporating both Type A and Type B contributions. Type B sources include distortion u_{dist}, binarization u_{bin}, filtration u_{fil}, and resolution u_{res}, while the Type A contribution u_{A} arises from temporal variation in the respective geometric parameter, as described in the Results. The combined standard uncertainty is calculated as:

$$u_{\mathrm{c}}(L_{\mathrm{px}}) = \sqrt{u_{\mathrm{dist}}^2(L_{\mathrm{px}}) + u_{\mathrm{bin}}^2(L_{\mathrm{px}}) + u_{\mathrm{fil}}^2(L_{\mathrm{px}}) + u_{\mathrm{res}}^2(L_{\mathrm{px}}) + u_{\mathrm{A}}^2(L_{\mathrm{px}})}, \tag{A1}$$

where L_{px} denotes the characteristic length in pixels, and the combined standard uncertainty is expressed in pixels. Distortion uncertainty is quantified using a checkerboard calibration target with a spatial tolerance of ±0.001 mm. Twenty images are acquired at different positions and angles for this quantification. Binarization and resolution uncertainties are assumed to have rectangular probability distribution, with contributions of two pixels per boundary and one pixel, respectively. To express the combined standard measurement uncertainty in millimeters, the pixel values must be multiplied by the calibration constant C. The law of propagation of uncertainty then gives this final expression:

$$u(L) = \sqrt{C^2 u_{\mathrm{c}}^2(L_{\mathrm{px}}) + L_{\mathrm{px}}^2 u^2(C)}, \tag{A2}$$

where $u(C)$ is the measurement uncertainty of the calibration constant, which must also be evaluated using the law of propagation of uncertainty, resulting in the equation:

$$u(C) = \sqrt{\left(\frac{1}{L_{\mathrm{ref,i,avg}}}\right)^2 u^2\left(L_{\mathrm{ref,r,avg}}\right) + \left(-\frac{L_{\mathrm{ref,r,avg}}}{L_{\mathrm{ref,i,avg}}^2}\right)^2 u^2\left(L_{\mathrm{ref,i,avg}}\right)}. \tag{A3}$$

The average characteristic length of the reference object in pixels is obtained from image measurements and denoted as $L_{\mathrm{ref,i,avg}}$, and $L_{\mathrm{ref,r,avg}}$ is the average characteristic length from repeated physical measurements of the reference object. Their standard deviations, $u(L_{\mathrm{ref,i,avg}})$ and $u(L_{\mathrm{ref,r,avg}})$, are calculated from these repetitions. We evaluate the measurement uncertainty of the calibration constant to be 5.06×10^{-5} mm px^{-1} and C as

5.65×10^{-3} mm px^{-1}. Using values calculated with Equation (A2), we calculate the relative standard uncertainty of film thickness and width:

$$u_\mathrm{R}(L) = \frac{u(L)}{L_\mathrm{avg}}. \tag{A4}$$

we calculate expanded measurement uncertainty as:

$$U = ku_\mathrm{R}(L);\ k = 2.000, \tag{A5}$$

where k is the coverage factor used to get 95.45% confidence level. To calculate the expanded measurement uncertainty of contact line positions, we use values calculated with Equation (A2):

$$U = ku(L);\ k = 2.000. \tag{A6}$$

References

1. Raupp, S.M.; Merklein, L.; Pathak, M.; Scharfer, P.; Schabel, W. An Experimental Study on the Reproducibility of Different Multilayer OLED Materials Processed by Slot Die Coating. *Chem. Eng. Sci.* **2017**, *160*, 113–120. [CrossRef]
2. Kim, G.; Na, J.; Jung, M.; Park, J. Structural Optimization of Slot-Die Heads with T-Shaped Cavity for Fabrication of Large-Area OLEDs. *Displays* **2023**, *80*, 102554. [CrossRef]
3. Li, J.; Fleetwood, J.; Hawley, W.B.; Kays, W. From Materials to Cell: State-of-the-Art and Prospective Technologies for Lithium-Ion Battery Electrode Processing. *Chem. Rev.* **2022**, *122*, 903–956. [CrossRef] [PubMed]
4. Spiegel, S.; Hoffmann, A.; Klemens, J.; Scharfer, P.; Schabel, W. High-Speed Slot-Die Coating of Primer Layers for Li-Ion Battery Electrodes: Model Calculations and Experimental Validation of the Extended Coating Window Depending on Coating Speed, Coating Gap and Viscosity. *J. Coat. Technol. Res.* **2024**, *21*, 493–505. [CrossRef]
5. Matondo, J.T.; Hu, H.; Ding, Y.; Mateen, M.; Cheng, G.; Ding, J. Slot-Die Coating for Scalable Fabrication of Perovskite Solar Cells and Modules. *Adv. Mater. Technol.* **2024**, *9*, 2302082. [CrossRef]
6. Bodner, M.; García, H.R.; Steenberg, T.; Terkelsen, C.; Alfaro, S.M.; Avcioglu, G.S.; Vassiliev, A.; Primdahl, S.; Hjuler, H.A. Enabling Industrial Production of Electrodes by Use of Slot-Die Coating for HT-PEM Fuel Cells. *Int. J. Hydrogen Energy* **2019**, *44*, 12793–12801. [CrossRef]
7. Stähler, M.; Stähler, A.; Scheepers, F.; Carmo, M.; Stolten, D. A Completely Slot Die Coated Membrane Electrode Assembly. *Int. J. Hydrogen Energy* **2019**, *44*, 7053–7058. [CrossRef]
8. Creel, E.B.; Tjiptowidjojo, K.; Alex Lee, J.; Livingston, K.M.; Randall Schunk, P.; Bell, N.S.; Serov, A.; Wood, D.L. Slot-Die-Coating Operability Windows for Polymer Electrolyte Membrane Fuel Cell Cathode Catalyst Layers. *J. Colloid Interface Sci.* **2022**, *610*, 474–485. [CrossRef]
9. Sharma, J.; Lyu, X.; Reshetenko, T.; Polizos, G.; Livingston, K.; Li, J.; Wood, D.L.; Serov, A. Catalyst Layer Formulations for Slot-Die Coating of PEM Fuel Cell Electrodes. *Int. J. Hydrogen Energy* **2022**, *47*, 35838–35850. [CrossRef]
10. Van Buskirk, G.A.; Gonzalez, M.A.; Shah, V.P.; Barnhardt, S.; Barrett, C.; Berger, S.; Cleary, G.; Chan, K.; Flynn, G.; Foster, T.; et al. Scale-up of Adhesive Transdermal Drug Delivery Systems. *Pharm. Res.* **1997**, *14*, 848–852. [CrossRef]
11. Alissa, I.; Nair, A.B.; Aldhubiab, B.; Shah, H.; Shah, J.; Mewada, V.; Almuqbil, R.M.; Jacob, S. Design, Development, and Evaluation of Treprostinil Embedded Adhesive Transdermal Patch. *Pharmaceutics* **2023**, *15*, 1226. [CrossRef]
12. Pantazoglou, E.; Tollemeto, M.; Ezazi, N.Z.; Chang, T.-J.; Hosta Rigau, L.; Jacobsen, J.; Hagner Nielsen, L. Enhancing Buccal Drug Delivery: The Impact of Glycerol in Slot-Die-Coated Pectin Films. *Mol. Pharm.* **2025**, *22*, 433–445. [CrossRef]
13. Merklein, L.; Mink, M.; Kourkoulos, D.; Ulber, B.; Raupp, S.M.; Meerholz, K.; Scharfer, P.; Schabel, W. Multilayer OLEDs with Four Slot Die-Coated Layers. *J. Coat. Technol. Res.* **2019**, *16*, 1643–1652. [CrossRef]
14. Verma, A.; Martineau, D.; Hack, E.; Makha, M.; Turner, E.; Nüesch, F.; Heier, J. Towards Industrialization of Perovskite Solar Cells Using Slot Die Coating. *J. Mater. Chem. C Mater.* **2020**, *8*, 6124–6135. [CrossRef]
15. Li, J.; Dagar, J.; Shargaieva, O.; Maus, O.; Remec, M.; Emery, Q.; Khenkin, M.; Ulbrich, C.; Akhundova, F.; Márquez, J.A.; et al. Ink Design Enabling Slot-Die Coated Perovskite Solar Cells with >22% Power Conversion Efficiency, Micro-Modules, and 1 Year of Outdoor Performance Evaluation. *Adv. Energy Mater.* **2023**, *13*, 2203898. [CrossRef]
16. Li, J.; Dagar, J.; Shargaieva, O.; Flatken, M.A.; Köbler, H.; Fenske, M.; Schultz, C.; Stegemann, B.; Just, J.; Többens, D.M.; et al. 20.8% Slot-Die Coated MAPbI3 Perovskite Solar Cells by Optimal DMSO-Content and Age of 2-ME Based Precursor Inks. *Adv. Energy Mater.* **2021**, *11*, 2003460. [CrossRef]

17. Diehm, R.; Müller, M.; Burger, D.; Kumberg, J.; Spiegel, S.; Bauer, W.; Scharfer, P.; Schabel, W. High-Speed Coating of Primer Layer for Li-Ion Battery Electrodes by Using Slot-Die Coating. *Energy Technol.* **2020**, *8*, 2000259. [CrossRef]
18. Beyerlein, K.R.; Dierksmeyer, D.; Mariani, V.; Kuhn, M.; Sarrou, I.; Ottaviano, A.; Awel, S.; Knoska, J.; Fuglerud, S.; Jönsson, O.; et al. Mix-and-Diffuse Serial Synchrotron Crystallography. *IUCrJ* **2017**, *4*, 769–777. [CrossRef] [PubMed]
19. Henkel, A.; Galchenkova, M.; Maracke, J.; Yefanov, O.; Klopprogge, B.; Hakanpää, J.; Mesters, J.R.; Chapman, H.N.; Oberthuer, D. JINXED: Just in Time Crystallization for Easy Structure Determination of Biological Macromolecules. *IUCrJ* **2023**, *10*, 253–260. [CrossRef]
20. Zielinski, K.A.; Prester, A.; Andaleeb, H.; Bui, S.; Yefanov, O.; Catapano, L.; Henkel, A.; Wiedorn, M.O.; Lorbeer, O.; Crosas, E.; et al. Rapid and Efficient Room-Temperature Serial Synchrotron Crystallography Using the CFEL TapeDrive. *IUCrJ* **2022**, *9*, 778–791. [CrossRef]
21. Prester, A.; Perbandt, M.; Galchenkova, M.; Oberthuer, D.; Werner, N.; Henkel, A.; Maracke, J.; Yefanov, O.; Hakanpää, J.; Pompidor, G.; et al. Time-Resolved Crystallography of Boric Acid Binding to the Active Site Serine of the β-Lactamase CTX-M-14 and Subsequent 1,2-Diol Esterification. *Commun. Chem.* **2024**, *7*, 152. [CrossRef] [PubMed]
22. Spiegel, S.; Hoffmann, A.; Klemens, J.; Scharfer, P.; Schabel, W. Optimization of Edge Quality in the Slot-Die Coating Process of High-Capacity Lithium-Ion Battery Electrodes. *Energy Technol.* **2023**, *11*, 2200684. [CrossRef]
23. Schmitt, M.; Scharfer, P.; Schabel, W. Slot Die Coating of Lithium-Ion Battery Electrodes: Investigations on Edge Effect Issues for Stripe and Pattern Coatings. *J. Coat. Technol. Res.* **2014**, *11*, 57–63. [CrossRef]
24. Huang, T.; Tan, P.; Zhong, Z.; Li, M.; Zhang, Y.; Zhou, H. Numerical and Experimental Investigation on the Defect Formation in Lithium-Ion-Battery Electrode-Slot Coating. *Chem. Eng. Sci.* **2022**, *258*, 117744. [CrossRef]
25. Pan, W.; Chen, Z.; Chen, X.; Wang, F.; Dai, G. Slot Die Coating Window for a Uniform Fuel Cell Ink Dispersion. *AIChE J.* **2022**, *68*, e17719. [CrossRef]
26. Park, J.; Kim, S.; Lee, C. An Analysis of Pinned Edge Layer of Slot-Die Coated Film in Roll-to-Roll Green Manufacturing System. *Int. J. Precis. Eng. Manuf.-Green Technol.* **2018**, *5*, 247–254. [CrossRef]
27. Park, J.; Shin, K.; Lee, C. Improvement of Cross-Machine Directional Thickness Deviation for Uniform Pressure-Sensitive Adhesive Layer in Roll-to-Roll Slot-Die Coating Process. *Int. J. Precis. Eng. Manuf.* **2015**, *16*, 937–943. [CrossRef]
28. Kang, H.; Park, J.; Shin, K. Statistical Analysis for the Manufacturing of Multi-Strip Patterns by Roll-to-Roll Single Slot-Die Systems. *Robot. Comput.-Integr. Manuf.* **2014**, *30*, 363–368. [CrossRef]
29. Diehm, R.; Weinmann, H.; Kumberg, J.; Schmitt, M.; Fleischer, J.; Scharfer, P.; Schabel, W. Edge Formation in High-Speed Intermittent Slot-Die Coating of Disruptively Stacked Thick Battery Electrodes. *Energy Technol.* **2020**, *8*, 1900137. [CrossRef]
30. Schmitt, M.; Baunach, M.; Wengeler, L.; Peters, K.; Junges, P.; Scharfer, P.; Schabel, W. Slot-Die Processing of Lithium-Ion Battery Electrodes—Coating Window Characterization. *Chem. Eng. Process. Process Intensif.* **2013**, *68*, 32–37. [CrossRef]
31. Spiegel, S.; Heckmann, T.; Altvater, A.; Diehm, R.; Scharfer, P.; Schabel, W. Investigation of Edge Formation during the Coating Process of Li-Ion Battery Electrodes. *J. Coat. Technol. Res.* **2022**, *19*, 121–130. [CrossRef]
32. Schweizer, P.M. Visualization of Coating Flows. *J. Fluid Mech.* **1988**, *193*, 285–302. [CrossRef]
33. Nam, J.; Carvalho, M.S. Flow Visualization and Operating Limits of Tensioned-Web-over Slot Die Coating Process. *Chem. Eng. Process. Process Intensif.* **2011**, *50*, 471–477. [CrossRef]
34. Chang, Y.R.; Chang, H.M.; Lin, C.F.; Liu, T.J.; Wu, P.Y. Three Minimum Wet Thickness Regions of Slot Die Coating. *J. Colloid Interface Sci.* **2007**, *308*, 222–230. [CrossRef]
35. Ji, H.S.; Ahn, W.G.; Kwon, I.; Nam, J.; Jung, H.W. Operability Coating Window of Dual-Layer Slot Coating Process Using Viscocapillary Model. *Chem. Eng. Sci.* **2016**, *143*, 122–129. [CrossRef]
36. Romero, O.J.; Suszynski, W.J.; Scriven, L.E.; Carvalho, M.S. Low-Flow Limit in Slot Coating of Dilute Solutions of High Molecular Weight Polymer. *J. Non-Newton. Fluid Mech.* **2004**, *118*, 137–156. [CrossRef]
37. Taylor, S.D.; Hrymak, A.N. Visualization and Flow Simulation of a Two-Layer Slot Coater. *Chem. Eng. Sci.* **1999**, *54*, 909–918. [CrossRef]
38. Hong, H.; Nam, J. Automatic Detection of Contact Lines in Slot Coating Flows. *AIChE J.* **2017**, *63*, 2440–2450. [CrossRef]
39. Kim, M.; Noh, J.; Cho, G.; Jo, J.; Lee, C. Predicting Quality of Coated Layer Based on Meniscus Features Associated with Thickness for Sustainable Roll-to-Roll Processes. *Int. J. Precis. Eng. Manuf.-Green Technol.* **2025**, *12*, 813–828. [CrossRef]
40. Sartor, L. Fluid Mechanics and Die Design. Ph.D. Thesis, University of Minnesota, Minneapolis, MN, USA, 1990.
41. McCauley, M. AccelStepper Library. Available online: https://www.airspayce.com/mikem/arduino/AccelStepper/ (accessed on 5 October 2021).
42. Bradski, G. The OpenCV Library. *Dr. Dobb's J. Softw. Tools Prof. Program* **2000**, *25*, 120–123.
43. Virtanen, P.; Gommers, R.; Oliphant, T.E.; Haberland, M.; Reddy, T.; Cournapeau, D.; Burovski, E.; Peterson, P.; Weckesser, W.; Bright, J.; et al. SciPy 1.0: Fundamental Algorithms for Scientific in Python. *Nat. Methods* **2020**, *17*, 261–272. [CrossRef] [PubMed]
44. Harris, C.R.; Millman, K.J.; van der Walt, S.J.; Gommers, R.; Virtanen, P.; Cournapeau, D.; Wieser, E.; Taylor, J.; Berg, S.; Smith, N.J.; et al. Array Programming with NumPy. *Nature* **2020**, *585*, 357–362. [CrossRef]

45. van der Walt, S.; Schönberger, J.L.; Nunez-Iglesias, J.; Boulogne, F.; Warner, J.D.; Yager, N.; Gouillart, E.; Yu, T. Scikit-Image: Image Processing in Python. *PeerJ* **2014**, *2*, e453. [CrossRef]
46. Hunter, J.D. Matplotlib: A 2D Graphics Environment. *Comput. Sci. Eng.* **2007**, *9*, 90–95. [CrossRef]
47. Otsu, N. A Threshold Selection Method from Gray-Level Histograms. *IEEE Trans. Syst. Man Cybern.* **1979**, *9*, 62–66. [CrossRef]
48. Schneider, C.A.; Rasband, W.S.; Eliceiri, K.W. NIH Image to ImageJ: 25 Years of Image Analysis. *Nat. Methods* **2012**, *9*, 671–675. [CrossRef]
49. Welch, B.L. The Generalisation of Student's Problems When Several Different Population Variances Are Involved. *Biometrika* **1947**, *34*, 28–35. [CrossRef]
50. Welch, B.L. The Significance of the Difference Between Two Means When the Population Variances Are Unequal. *Biometrika* **1938**, *29*, 350–362. [CrossRef]
51. Satterthwaite, F.E. Synthesis of Variance. *Psychometrika* **1941**, *6*, 309–316. [CrossRef]
52. Joint Committee for Guides in Metrology. *Evaluation of Measurement Data—Guide to the Expression of Uncertainty in Measurement*; JCGM 100:2008; Bureau International des Poids et Mesures (BIPM): Sèvres, France, 2008.
53. Kovačič, K.; Gregorc, J.; Šarler, B. Numerical Modelling and Experimental Validation of Dripping, Jetting and Whipping Modes of Gas Dynamic Virtual Nozzle. *Int. J. Numer. Methods Heat Fluid Flow* **2024**, *34*, 1582–1608. [CrossRef]
54. Zupan, B.; Peña-Murillo, G.E.; Zahoor, R.; Gregorc, J.; Šarler, B.; Knoška, J.; Gañán-Calvo, A.M.; Chapman, H.N.; Bajt, S. An Experimental Study of Liquid Micro-Jets Produced with a Gas Dynamic Virtual Nozzle under the Influence of an Electric Field. *Front. Mol. Biosci.* **2023**, *10*, 1006733. [CrossRef] [PubMed]
55. Zupan, B.; Bajt, S.; Chapman, H.N.; Šarler, B. Acceleration of Flow-Focused Liquid Jets in the Presence of a Strong Electric Field. *J. Phys. Conf. Ser.* **2024**, *2766*, 012070. [CrossRef]
56. Vidic, G.; Zupan, B.; Kovačič, K.; Velnar, V.; Bajt, S.; Šarler, B. Analysis of Liquid Sample Delivery Shapes Employing Computer Vision. *Mech. Eng. World* **2024**, *13*, 162–163. [CrossRef]